Oscillation analysis in Hall thrusters with 2D (axial-azimuthal) Particle-In-Cell simulations

Thomas Charoy, A. Bourdon, Pascal Chabert, Trevor Lafleur, Antoine Tavant

Oscillation analysis in Hall thrusters with 2D (axial-azimuthal) Particle-In-Cell simulations

IEPC-2019-A487

Presented at the 36th International Electric Propulsion Conference
University of Vienna, Austria
September 15-20, 2019

T. Charoy*, A. Bourdon†and P. Chabert ‡
Laboratoire de Physique des Plasmas (LPP), CNRS, Ecole polytechnique,
Sorbonne Universités, Université Paris-Sud, Observatoire de Paris, Université Paris-Saclay,
PSL Research University, 91128 Palaiseau, France
and

T. Lafleur§
PlasmaPotential-Physics Consulting and Research, Canberra, ACT 2601, Australia
and

A. Tavant¶
Safran Aircaft Engines, Vernon, France
Laboratoire de Physique des Plasmas (LPP), CNRS, Ecole polytechnique,
Sorbonne Universités, Université Paris-Sud, Observatoire de Paris, Université Paris-Saclay,
PSL Research University, 91128 Palaiseau, France

The two-dimensional Particle-In-Cell code *LPPic* is used to simulate self-consistently the axial-azimuthal plane of a Hall Thruster. Axial breathing mode oscillations are observed and their interactions with the azimuthal Electron Cyclotron Drift Instability (ECDI) are discussed. It appears that the ECDI grows when the discharge current increases and this growth is associated with an increase of the electron-ion friction force that greatly contributes to the axial anomalous electron transport. In these simulations, the vacuum permittivity constant is artificially increased to reduce computational time. The influence of this scaling technique on the axial and azimuthal instabilities and the electron axial transport is studied. The correlation between an increase of the vacuum permittivity and the decrease of the electron-ion friction force (and hence the electron axial transport) is shown.

*Ph.D. student, thomas.charoy@lpp.polytechnique.fr
†Research director, Centre National de la Recherche Scientifique, anne.bourdon@lpp.polytechnique.fr
‡Research director, Centre National de la Recherche Scientifique, pascal.chabert@lpp.polytechnique.fr
§Physics consultant, PlasmaPotential, trevor.lafleur@plasmapotential.com.au
¶Ph.D. student, antoine.tavant@lpp.polytechnique.fr

Nomenclature

x, y, z = axial, azimuthal and radial directions
Δt = time step
Δx = cell size
L_x, N_x = domain length and number of cells in axial direction
L_y, N_y = domain length and number of cells in azimuthal direction
$x_{B_{max}}$ = axial position of radial magnetic field maximum (thruster exit plane)
N_{ppc} = number of macroparticles per cell
ϵ_0 = vacuum permittivity
k_B = Boltzmann constant
α_ϵ = vacuum permittivity scaling factor
n_e = electron density
T_e = electron temperature
m = electron mass
n_g = neutral density (Xenon)
v_g = neutral velocity (Xenon)
T_g = neutral temperature (Xenon)
E_g = neutral total energy per volume (Xenon)
$\dot{m}$ = anode neutral mass flow rate (Xenon)
S_{iz} = ionization source term
B = radial (imposed) magnetic field
I_d = discharge current

F_B = Magnetic term (electron momentum conservation equation)
F_t = Temporal inertia term (electron momentum conservation equation)
F_{in} = Spatial inertia term (electron momentum conservation equation)
F_p = Pressure term (electron momentum conservation equation)
F_E = Electric term (electron momentum conservation equation)
F_{en} = Electron-neutral momentum collision term (electron momentum conservation equation)
F_{ei} = Electron-ion friction force term (electron momentum conservation equation)

HET = Hall-effect thruster
PIC = Particle-In-Cell
MCC = Monte-Carlo Collisions
CPU = Central Processing Unit
MPI = Message Passing Interface
FFT = Fast Fourier Transform

I. Introduction

Hall Effect Thrusters (HET) have been widely used for spacecraft propulsion in the last decade. These cylindrical devices produce thrust by accelerating ions through an axial electric field $\boldsymbol{E}$ originating from an imposed potential difference between an anode and a cathode. The ionization efficiency is enhanced by a radial magnetic field $\boldsymbol{B}$ that confines electrons emitted from the cathode. These electrons are drifting in the azimuthal direction with a large $\boldsymbol{E}\mathrm{x}\boldsymbol{B}$ velocity.

Even though many studies[1,2] have been conducted on these devices, some key features are still not well understood. One of the most important might be the electron axial transport across the magnetic field. It has been experimentally observed[3] that the electron mobility across the discharge chamber is higher than the one expected with the classical collisional theory. This axial transport should be reduced to increase thruster performances but to do so, we need to understand where it comes from. Recent numerical simulations[4,5] have shown that Electron Cyclotron Drift Instabilities (ECDI) could be a main cause of this anomalous transport. These instabilities are characterized by a short wavelength in the mm range and a high frequency in the MHz range. They might be related to low-frequency (10-30 kHz) axial oscillations of the discharge current, known as the breathing mode oscillations.[6] Many other instabilities can be observed in a HET, with a wide range of frequencies[7,8] and they might also affect the discharge behavior.

As these instabilities are kinetic in nature, Particle-In-Cell (PIC) codes are needed to understand its origin and how they influence the discharge behaviour. However, the parameters of a PIC simulation need to comply to the well-known stability criteria: $w_p\Delta t \leq 0.2$ and $\Delta x \leq \lambda_d$, with $w_p = \sqrt{\frac{n_e e^2}{m\epsilon_0}}$ and $\lambda_d = \sqrt{\frac{\epsilon_0 k_B T_e}{n_e e^2}}$ being respectively the plasma pulsation and Debye length. It gives:

$$\begin{cases} \Delta t \leq 0.2\sqrt{\dfrac{m\epsilon_0}{n_e e^2}} \\ \Delta x \leq \sqrt{\dfrac{\epsilon_0 k_B T_e}{n_e e^2}} \end{cases} \tag{1}$$

with n_e, T_e, m, e, k_B and ϵ_0 being respectively the electron density, temperature, mass, charge, the Boltzmann constant and the vacuum permittivity. As the electron density can be higher than $\approx 10^{18}$ m^{-3}, the numerical parameters can be as small as $\approx 10^{-12}$ s for the time step and $\approx 10^{-5}$ m for the cell size. Hence, 2D simulations require important computational resources while 3D simulations of a real HET configuration are currently out of scope.

To decrease the required computational time, scaling techniques can be used, such as decreasing the electron-ion mass ratio[9] or using a geometrical scaling factor.[10] Another scaling technique used by Szabo[9] for 2D axial-radial PIC simulations and more recently by Coche and Garrigues[11] for 2D axial-azimuthal PIC simulations, is the scaling of vacuum permittivity. Looking at the criteria of equations 1, it appears that increasing the vacuum permittivity ϵ_0 allows to use bigger time step and cell size, and hence reduce computational time, while keeping the stability. For a scaling factor α_ϵ such as $\epsilon_0' = \alpha_\epsilon \times \epsilon_0$, we can use $(\Delta x)' = \sqrt{\alpha_\epsilon}\Delta x$ and $(\Delta t)' = \sqrt{\alpha_\epsilon}\Delta t$. In Ref.[11] , α_ϵ was set to 80. Here, we use 4 values of α_ϵ : 4, 16, 64 and 256.

In this paper, we will first describe the simulation model and the chosen algorithms in section II. The results for the case with lower α_ϵ (closer to a real case) will then be presented in section III, before studying in section IV the influence of the vacuum permittivity scaling factor α_ϵ.

II. Model description

The 2D-3V Particle-In-Cell Monte Carlo collision (PIC-MCC) code *LPPic* has been used for this study. After being verified by a 1D Helium benchmark[12] , the radial-azimuthal plane of a HET have been extensively studied[13–15] with this code. Recently, a 2D axial-azimuthal benchmark for $\boldsymbol{E}\mathrm{x}\boldsymbol{B}$ discharges has been successfully performed to verify *LPPic* against 6 other independently developed codes[16] on a simulation model closer to a real HET discharge.

The axial (x) and azimuthal (y) directions of a HET are simulated, with a structured Cartesian mesh shown in figure 1. The axial domain of length $L_x = 4$ cm is delimited by an anode with an imposed potential of 300 V (x = 0 cm) and a cathode with an imposed potential of 0 V (x = L_x = 4 cm). The axial profile of the imposed radial magnetic field is displayed on figure 2 and the position of its maximum corresponds

to the exit plane of the thruster. To reduce computational times, only a small part of the HET azimuthal direction is simulated (L_y = 1 cm) and periodic boundary conditions are imposed in this direction. As the breathing mode frequency is around 20 kHz, the simulation cases have been run to at least 150 μs to capture several periods of the breathing mode oscillations.

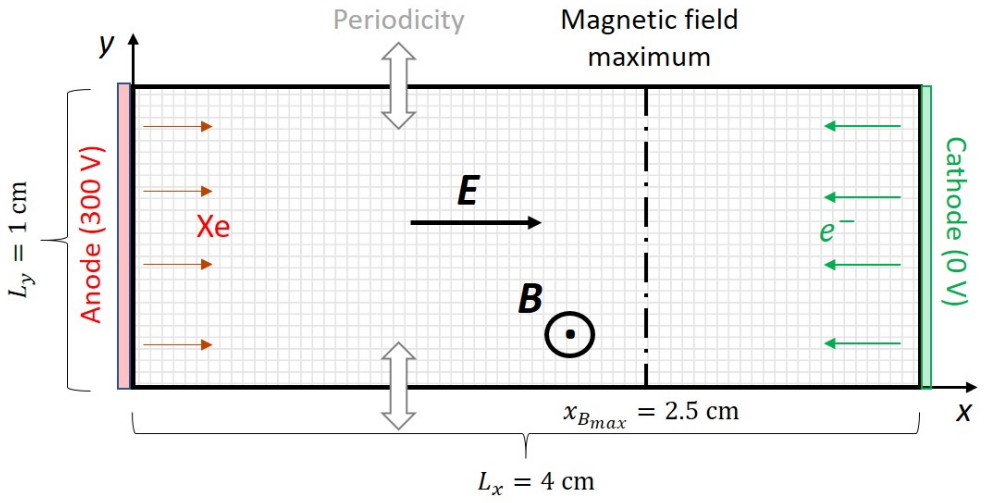

Figure 1: Simulation domain. x is the axial direction, y the (periodic) azimuthal direction. Black pointed dashed line ($x_{B_{max}}$=2.5 cm): position of maximum radial magnetic field. Xenon atoms are injected at the cathode and electrons are emitted from the cathode.

Because of the breathing mode oscillations, the plasma density can vary by almost a factor 5 (from $n_e \approx 5\times10^{17}$ m^{-3} to $n_e \approx 2.5\times10^{18}$ m^{-3}). When the plasma density is maximum, the electron temperature is around 40 eV. Hence, to comply with the PIC stability criteria of equations 1, the time step Δt and the cell size Δx has been fixed to 2×10^{-12} s and 2×10^{-5} m, respectively. It gives a computational mesh of N_x=2000 cells in the axial direction and N_y=512 cells in the azimuthal direction. At initialisation, the particles are loaded uniformly with a density of $n_{p,ini}$= 10^{18} m^{-3} and the initial number of macroparticles per cell has been fixed at 400 to reduce numerical noise.

Contrary to the simplified simulation case used in Ref.[16] , electron-neutral and ion-neutral collisions are taken into account (as described in Ref.[17]) and the ionization is calculated self-consistently. The Xenon neutral gas is considered as a fluid and any azimuthal variation is neglected. Hence, the 1D Euler equations for the neutrals are:

$$\begin{cases} \partial_t n_g + \partial_z(n_g v_g) = -S_{iz} \\ \partial_t(n_g v_g) + \partial_z(n_g v_g^2) = -\partial_z p_g - u_g S_{iz} \\ \partial_t E_g + \partial_z(E_g u_g) = -\partial_z(p_g u_g) \end{cases} \tag{2}$$

with n_g, u_g, p_g and E_g being respectively the neutral density, velocity, pressure and total energy per unit volume, and S_{iz} the ionization source term.

Equations 2 for the neutral gas are solved with a HLLC Riemann solver. The initial neutral density axial profile is displayed in figure 2 and the initial neutral velocity is considered uniform and equal to 200 m.s^{-1}. The neutral temperature is kept constant by adding a thermal relaxation source term to the energy equation. The neutral mass flow rate at the anode is fixed at $\dot{m}$= 5 mg.s^{-1}. These parameters, along with the radial magnetic field profile, are similar to those used by Lafleur *et al*[18] in which only the neutral continuity equation was solved and a constant axial velocity of the neutral gas was then assumed.

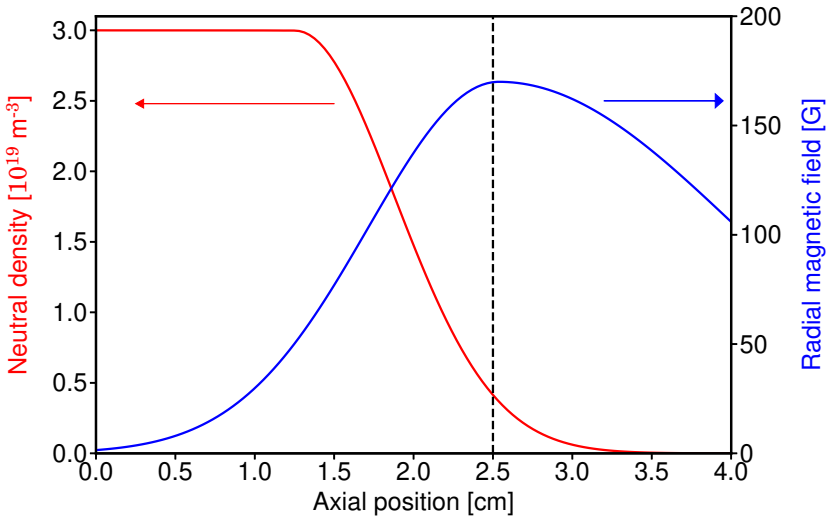

Figure 2: Axial profiles of the imposed radial magnetic field and initial neutral density. Dashed line corresponds to the position of maximum radial magnetic field.

The electron emission at the cathode to sustain the discharge is treated differently than in Refs.[11,16] in which a current equality into the whole system was considered. Indeed, as mentioned already in previous work[9,18] , this cathode model appears to create a cathode sheath and violate the current conservation during any transient state. Hence, we inject electrons according to a quasi-neutrality assumption: at each time step, the charge difference between ions and electrons at the right domain boundary (cathode) is calculated and if this charge difference is positive, the corresponding number of electrons is injected uniformly to neutralize it. If the charge difference is negative, no electron is emitted.

As mentioned before, we simulated here 4 cases with different values of the vacuum permittivity scaling factor: $\alpha_\epsilon = 4$, 16, 64 and 256. Hence, the time step and cell size has been increased by a corresponding factor of $\sqrt{\alpha_\epsilon}$ (while keeping the same axial and azimuthal length) which reduces significantly the computational time. Despite this scaling technique, the code needed to be parallelized for the cases to be simulated in a reasonable amount of time. The MPI (Message Passing Interface) protocol is used, with each CPU considering one portion of the simulation domain (domain decomposition approach). As described by Charoy *et al.*,[16] an electron subcycling technique along with a load balancing algorithm are used. The simulation cases remain very computationally expensive, with the longest case taking up to two months on 1120 CPUs.

III. Discharge behaviour

The simulation case with $\alpha_\epsilon = 4$, i.e. the case closer to a real case, is considered here. The simulation has been run until 150 μs and we have obtained a representative peak of discharge current that is used to analyse the discharge behaviour during a breathing mode cycle.

A. Breathing mode and ECDI

In a HET, the discharge current I_d corresponds to the anodic current, i.e. to the sum of the electron and ion currents collected at the anode. The time evolution of I_d is plotted in figure 3. After a transient regime characterized by two high-amplitude peaks, the discharge current oscillations get more steady. The corresponding frequency is 20 kHz. One can notice that two distinct regimes can be identified during one oscillation cycle: I_d grows in a short time and no additional oscillations are observed (regime I), while it decreases in a longer time with high frequency oscillations of the order of hundreds kHz (regime II). These oscillations have been observed previously in Ref.[11] and could be associated to ion-transit time instabilities.

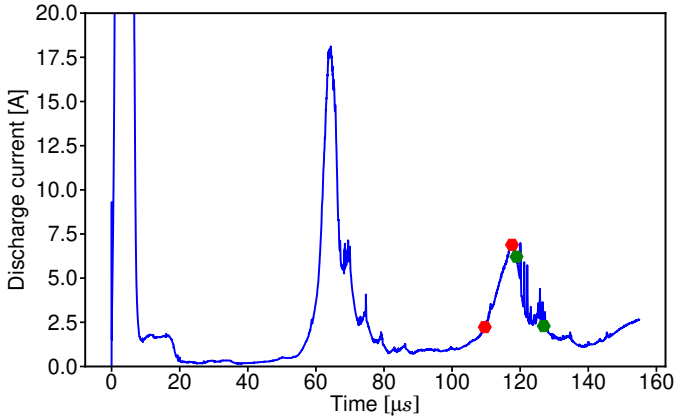

Figure 3: Time evolution of discharge current for α_ϵ=4. Markers correspond to the time interval chosen in figure 4 for the top row (red) and the bottom row (green).

Instabilities propagating in the azimuthal direction are studied for these two regimes. In figure 4, two snapshots of the azimuthal electric field are shown. The first row corresponds to regime I (growth) and the second row to regime II (decrease). 2D FFTs inside the thruster (x = 1 cm) and at the exit plane (x = 2.5 cm) have been calculated and are displayed on the corresponding row. We can see that the behaviour inside the thruster is quite similar, with short-wavelength ($\lambda \approx 0.5$ mm) and high frequency (f $\approx$ 5 MHz) waves that are characteristic of the ECDI. The amplitude of the azimuthal electric field oscillations is not displayed for clarity purpose but we observed that it is twice higher in regime I, which seems to correspond to the regime associated with the wave growth. The simulation performed by Lafleur *et al.*[18] was showing the same behaviour for a real case without any vacuum permittivity scaling but with only the beginning of regime I simulated.

The ion-acoustic dispersion relation $\omega = f(k)$ has been displayed on the 2D FFTs of figure 4, along with its corresponding growth rate γ:

$$\begin{cases} \omega \approx \boldsymbol{k}.\boldsymbol{v_{di}} \pm \dfrac{kc_s}{\sqrt{1+k^2\lambda_d^2}} \\ \gamma \approx \pm\sqrt{\dfrac{\pi m}{8M}}\dfrac{\boldsymbol{k}.\boldsymbol{v_{de}}}{(1+k^2\lambda_d^2)^{3/2}} \end{cases} \tag{3}$$

with M the ion mass, v_{di} the axial ion drift velocity, v_{de} the azimuthal electron drift velocity and c_s the ion sound speed. We observe that inside the thruster, the wave exhibits an ion-acoustic behaviour. However, outside the thruster the wave is not monochromatic anymore and a long-wavelength wave develops during regime II and is convected very quickly axially. More analysis need to be performed on the wave characteristics in this regime, near the exit plane and in the plume.

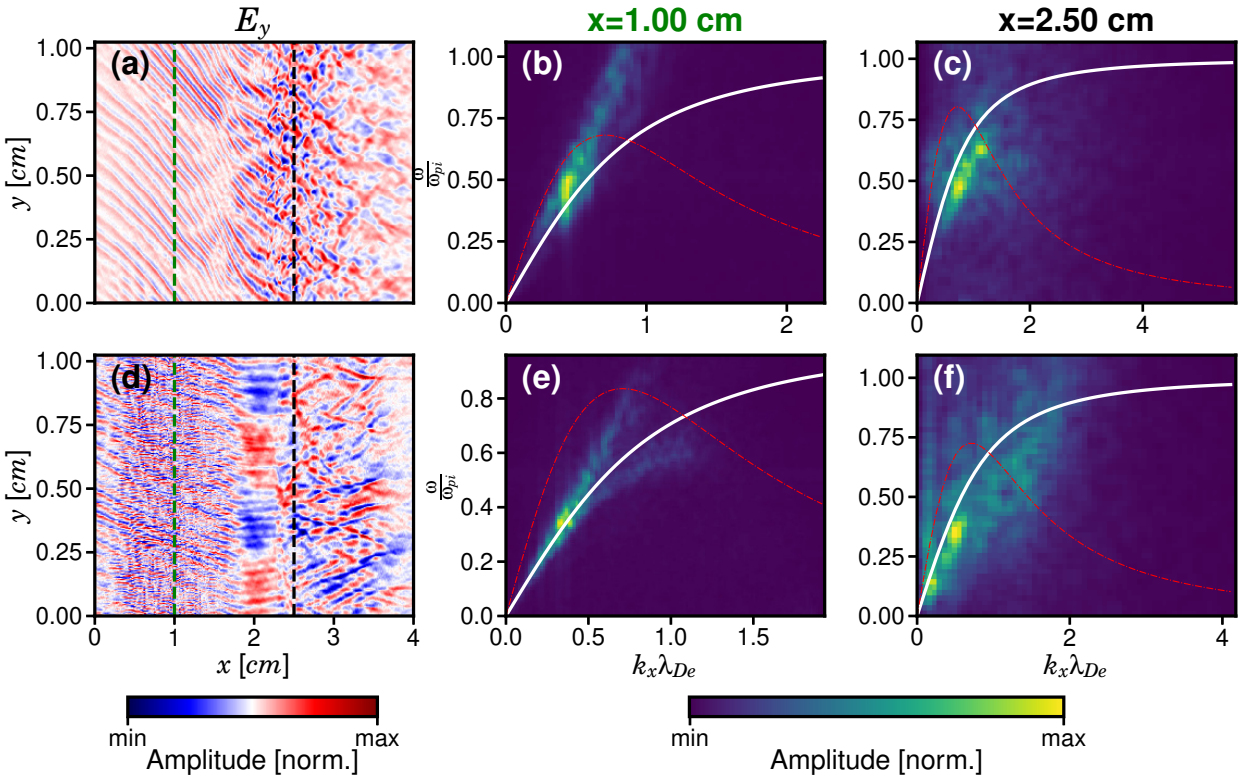

Figure 4: Left column: 2D snapshots of azimuthal electric field during peak growth (a, top row) and peak decrease (d, bottom row). Middle column: corresponding 2D FFT at x = 1 cm (green dashed line of left column). Right column: corresponding 2D FFT at x = 2.5 cm (black dashed line of left column). White thick line: ion-acoustic dispersion relation. Red dashed line: ion-acoustic growth rate rescaled by a constant factor to fit the image. The time interval chosen for the 2D FFT are shown in figure 3.

B. Axial electron transport

As mentioned earlier, the electron axial transport is still not well understood even though it has a major impact on the thruster performances. Similarly to what has been done in Ref.[18] , we consider here the electron momentum conservation equation in the axial and azimuthal direction, that gives respectively:

$$\begin{cases} qn_e v_{e,y} B = \partial_t(mn_e v_{e,x}) + \partial_x(mn_e v_{e,x}^2) + \partial_x(\Pi_{e,xx}) - qn_e E_x - R_{en,x} - R_{ei,x} \\ qn_e v_{e,x} B = \partial_t(mn_e v_{e,y}) + \partial_x(mn_e v_{e,x} v_{e,y}) + \partial_x(\Pi_{e,xy}) - qn_e E_y - R_{en,y} - R_{ei,y} \end{cases} \quad (4)$$

If we define $F_{B,x} = qn_e v_{e,y} B$ and $F_{B,y} = qn_e v_{e,x} B$ respectively the axial and azimuthal magnetic term, $F_{t,x} = \partial_t(mn_e v_{e,x})$ and $F_{t,y} = \partial_t(mn_e v_{e,y})$ respectively the axial and azimuthal temporal inertia term, $F_{in,x} = \partial_x(mn_e v_{e,x}^2)$ and $F_{in,y} = \partial_x(mn_e v_{e,x} v_{e,y})$ respectively the axial and azimuthal spatial inertia term, $F_{p,x} = \partial_x(\Pi_{e,xx})$ and $F_{p,y} = \partial_x(\Pi_{e,xy})$ respectively the axial and azimuthal pressure term, $F_{E,x} = -qn_e E_x$ and $F_{E,y} = -qn_e E_y$ respectively the axial and azimuthal electric term, $F_{en,x} = -R_{en,x}$ and $F_{en,y} = -R_{en,y}$ respectively the axial and azimuthal electron-neutral momentum collision term and $F_{ei,x} = -R_{ei,x} = -q < \delta n_e \delta E_x >$ and $F_{ei,y} = -R_{ei,y} = -q < \delta n_e \delta E_y >$ respectively the axial and azimuthal electron-ion friction force term; the above equations become in both directions:

$$F_B = F_t + F_{in} + F_p + F_E + F_{en} + F_{ei} \quad (5)$$

The different terms of the azimuthal equation are displayed in figure 5 which shows the different contributions to the electron axial velocity at two different times of a breathing mode cycle. The right hand-side of equation 5 is shown (SUM curve) to be equal to the left hand-side. The $F_{ei,y}$ term (cyan curve) corresponds to the drag force on the electrons, enhanced by the instabilities propagating in the azimuthal direction. When the discharge current is minimum, the electron axial velocity is low and even though the electron-ion

friction force $F_{ei,y}$ is not negligible, the main contribution for the axial electron transport are the electron-neutral collisions $F_{en,y}$ that are predominant inside the thruster. However, when the discharge current is maximum, the axial electron transport is greatly enhanced (by almost one order of magnitude), mainly by the electron-ion friction force that contributes more than the electron-neutral collisions. In both cases, the friction force is always dominant in the plume where the neutral density is low and the electron-neutral collisions are scarce.

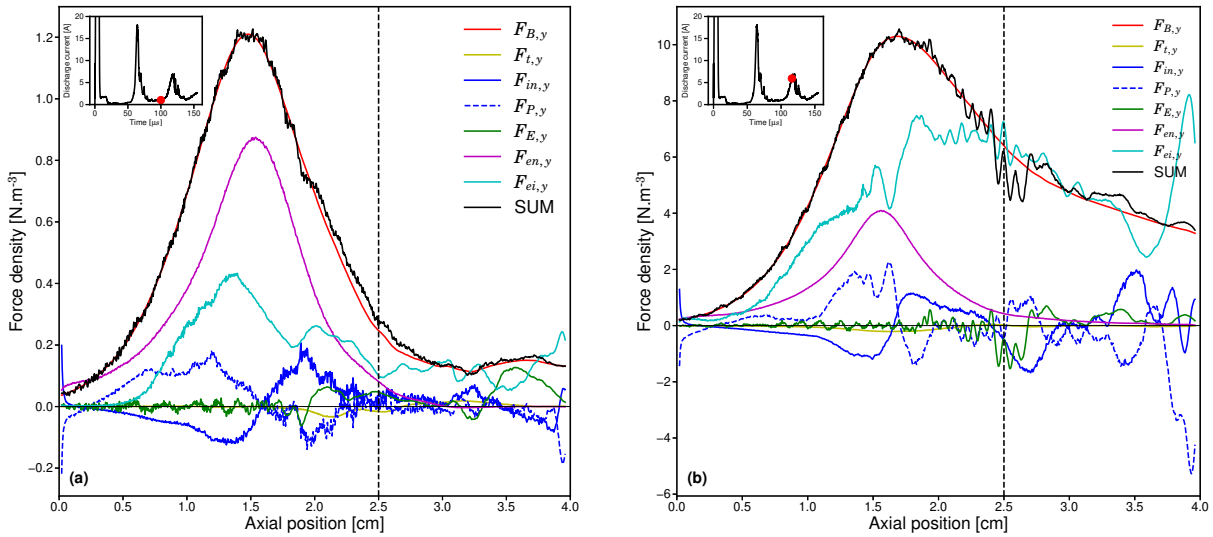

(a) At discharge current minimum

(b) At discharge current maximum

Figure 5: Azimuthal terms of electron momentum conservation equation 5 for two times of a breathing mode cycle, if $\alpha_\epsilon = 4$. The black line ("SUM") corresponds to the sum of the right hand-side terms of equation 5. The cyan $F_{ei,y}$ line corresponds to the instability-enhanced drag force on the electrons. Inset: Time evolution of discharge current, red dot indicating the corresponding time.

Hence, we have shown that the instability-enhanced electron-ion friction force is the main contributor to the electron axial transport. When the discharge current increases, the azimuthal instabilities amplitude grows and it enhances this electron-ion friction force: its relative importance to the electron axial transport is increased compared to the classical electron-neutral collisions.

IV. Influence of vacuum permittivity scaling

A 2D PIC simulation without any artificial scaling requires very important computational resources. It is then important to characterize how the use of a scaling on the vacuum permittivity would impact the discharge in order to know in what extent it could be used to study HET discharges.

The discharge current time evolution for 4 values of α_ϵ is shown in figure 6. We can see that we retrieved a similar breathing mode frequency of 20kHz but the oscillation amplitude seems to be damped when α_ϵ is increased.

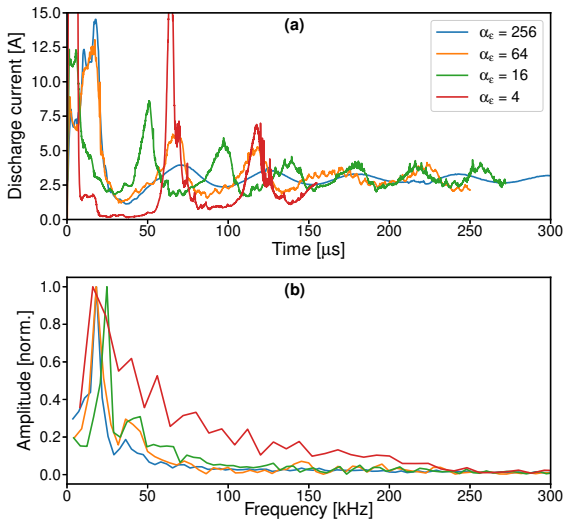

Figure 6: Time evolution of discharge current (a) and corresponding FFT (b), for 4 values of α_ϵ.

The azimuthal terms of the electron momentum conservation equation for $\alpha_\epsilon = 16$ and $\alpha_\epsilon = 64$ when the discharge current is maximum, are shown in figure 7. We can notice that when α_ϵ is increased, the electron axial transport is decreased and the electron-neutral collisions become the dominant contribution to this transport, with a significant decrease of the electron-ion friction force. It is interesting to note that the electron-neutral momentum collisions looks almost constant with α_ϵ.

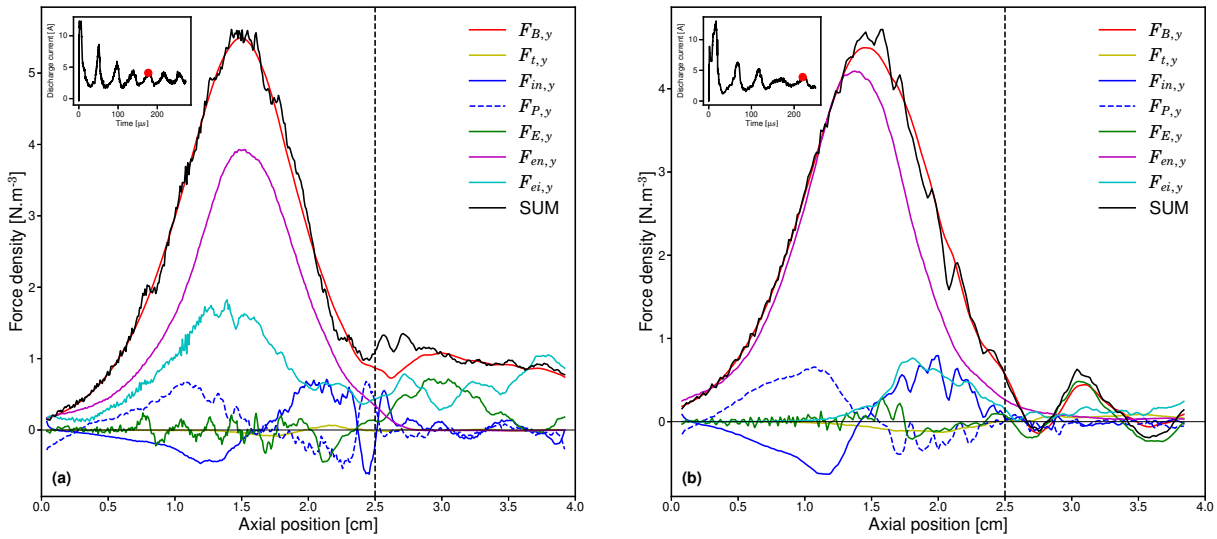

(a) $\alpha_\epsilon = 16$ (b) $\alpha_\epsilon = 64$

Figure 7: Azimuthal terms of electron momentum conservation equation at a discharge current maximum for two values of α_ϵ. The black line ("SUM") corresponds to the sum of the right hand-side terms of equation 5. The cyan $F_{ei,y}$ line corresponds to the instability-enhanced drag force on the electrons. Inset: Time evolution of discharge current, red dot indicating the friction force diagnostic time.

If we average over 2 breathing mode cycles, we observe in figure 8 that an increase of the vacuum permittivity scaling factor results in a significant decrease of the electron-ion friction force. This behaviour was predicted by the theory developed in Lafleur *et al*[19] where the expected ECDI growth rate was inversely proportional to the Debye length as shown in equation 3. An increase of the vacuum permittivity damps the growth rate, whereas the instability convection rate remains the same (it proceeds at the wave group velocity which is close to the axial ion drift velocity). Hence, the instability amplitude at equilibrium is expected to be lower and so is the friction force.

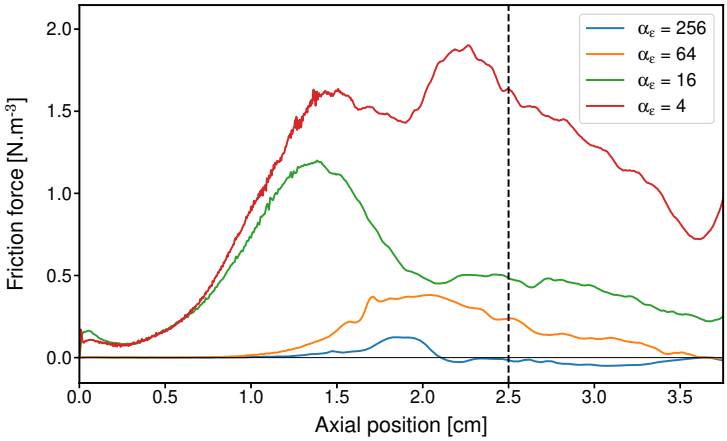

Figure 8: Axial profiles of electron-ion friction force averaged over 2 breathing mode cycles, for different values of α_ϵ. Dashed line corresponds to the position of maximum radial magnetic field.

V. Conclusion

In this paper, two-dimensional axial-azimuthal Particle-In-Cell simulations have been performed with a self-consistent ionization obtained via a Monte Carlo Collision module and the neutral dynamic solved at each time step. Low-frequency axial oscillations of the breathing mode have been observed and their coupling with azimuthal high-frequency oscillations known as ECDI has been discussed. We have observed that the growth of these azimuthal instabilities is associated with an increase of the discharge current in the thruster. This growth enhances the so-called electron-ion friction force that enhances in return the axial electron transport. We have shown that this friction force is the main contributor for the observed axial electron anomalous transport during the discharge current increase and maximum, while the classical collisional transport is dominant when the discharge current is low.

These results have been obtained by artificially increasing the vacuum permittivity by a factor α_ϵ in order to reduce computational time. This scaling technique is still needed to perform self-consistent 2D simulations of a HET. Its impact on the discharge behaviour and more specifically on the azimuthal instabilities and axial electron transport has been discussed. As expected by previous theoretical works, increasing the vacuum permittivity damps the ECDI growth and hence, reduces the electron-ion friction force, which results in a decrease of the axial electron transport.

More analysis need to be performed on the characterization of the azimuthal instabilities when the discharge current decreases and ideally, a different simulation case needs to be found (which gives lower plasma densities), in order to be used to simulate a real case without any scaling.

Acknowledgments

T.C., A.B. and P.C. acknowledge support from the Agence Nationale de la Recherche under the reference ANR-16-CHIN-0003-01 and Safran Aircraft Engines within the project POSEIDON. They also acknowledge access to the HPC resources of CINES (under the allocation A0040510092 made by GENCI) and of CERFACS at Toulouse.

References

[1]Adam, J., Boeuf, J.-P., Dubuit, N., Dudeck, M., Garrigues, L., Gresillon, D., Heron, A., Hagelaar, G., Kulaev, V., Lemoine, N., Mazouffre, S., Luna, J. P., Pisarev, V., and Tsikata, S., "Physics, simulation and diagnostics of Hall effect thrusters," *Plasma Phys. Control. Fusion*, Vol. 50, 2008, pp. 124041.

[2]Boeuf, J., "Tutorial : Physics and modeling of Hall thrusters," *J. Appl. Phys.*, Vol. 121, 2017, pp. 011101.

[3]Meezan, N., Jr, W. H., and Cappelli, M., "Anomalous electron mobility in a coaxial Hall discharge plasma," *Phys. Rev. E*, Vol. 63, 2001, pp. 026410.

[4]Adam, J. C., Heron, A., and Laval, G., "Study of stationary plasma thrusters using two-dimensional fully kinetic simulations," *Phys. Plasmas*, Vol. 11, No. 1, 2004, pp. 295–305.

[5]Lafleur, T., Baalrud, S. D., and Chabert, P., "Theory for the anomalous electron transport in Hall effect thrusters. I. Insights from particle-in-cell simulations," *Phys. Plasmas*, Vol. 23, No. 5, 2016, pp. 053502.

[6]Barral, S. and Ahedo, E., "Low-frequency model of breathing oscillations in Hall discharges," *Phys. Rev. E*, Vol. 79, 2009, pp. 046401.

[7]Choueiri, E., "Plasma oscillations in Hall thrusters," *Phys. Plasmas*, Vol. 8, 04 2001, pp. 1411.

[8]Smolyakov, A., Chapurin, O., Frias Pombo, W., Koshkarov, O., Romadanov, I., Tang, T., Umansky, M., Raitses, Y., Kaganovich, I., and Lakhin, V., "Fluid theory and simulations of instabilities, turbulent transport and coherent structures in partially-magnetized plasmas of $\mathbf{E} \times \mathbf{B}$ discharges," *Plasma Physics and Controlled Fusion*, Vol. 59, 01 2017, pp. 014041.

[9]Szabo, J. J., *Fully Kinetic Numerical Modeling of a Plasma Thruster*, Ph.D. thesis, Massachusetts Institute of Technology, 2011.

[10]Taccogna, F. and Minelli, P., "Three-dimensional particle-in-cell model of Hall thruster: The discharge channel," *Physics of Plasmas*, Vol. 25, No. 6, 2018, pp. 061208.

[11]Coche, P. and Garrigues, L., "A Two-dimensional (azimuthal-axial) Particle-In-Cell model of a Hall Thruster," *Phys. Plasmas*, Vol. 21, 2014, pp. 023503.

[12]Turner, M., Derzsi, A., Donkó, Z., Eremin, D., Kelly, S., Lafleur, T., and Mussenbrock, T., "Simulation benchmarks for low-pressure plasmas: Capacitive discharges," *Phys. Plasmas*, Vol. 20, 2013, pp. 013507.

[13]Croes, V., Lafleur, T., Bonaventura, Z., Bourdon, A., and Chabert, P., "2D particle-in-cell simulations of the electron drift instability and associated anomalous electron transport in Hall-effect thrusters," *Plasma Sources Sci. Technol.*, Vol. 26, 2017, pp. 034001.

[14]Croes, V., Tavant, A., Lucken, R., Martorelli, R., Lafleur, T., Bourdon, A., and Chabert, P., "The effect of alternative propellants on the electron drift instability in Hall-effect thrusters: Insight from 2D particle-in-cell simulations," *Phys. Plasmas*, Vol. 25, 2018, pp. 063522.

[15]Tavant, A., Croes, V., Lucken, R., Lafleur, T., Bourdon, A., and Chabert, P., "The effects of secondary electron emission on plasma sheath characteristics and electron transport in an $\mathbf{E} \times \mathbf{B}$ discharge via kinetic simulations," *Plasma Sources Sci. Technol.*, Vol. 27, 2018, pp. 12.

[16]Charoy, T., Boeuf, J., Bourdon, A., Carlsson, J., Chabert, P., Cuenot, B., Eremin, D., Garrigues, L., Hara, K., Kaganovich, I., Powis, T., Smolyakov, A., Sydorenko, D., Tavant, A., Vermorel, O., and Villafana, W., "2D axial-azimuthal Particle-In-Cell benchmark for low-temperature partially magnetized plasmas," *in revision Plasma Sources Sci. Technol.*, 2019.

[17]Croes, V., *Modélisation bidimensionnelle de la décharge plasma dans un propulseur de Hall*, Ph.D. thesis, Université Paris-Saclay, France, 2017.

[18]Lafleur, T. and Chabert, P., "The role of instability-enhanced friction on 'anomalous' electron and ion transport in Hall-effect thrusters," *Plasma Sources Sci. Technol.*, Vol. 27, 2018, pp. 015003.

[19]Lafleur, T., Baalrud, S. D., and Chabert, P., "Theory for the anomalous electron transport in Hall effect thrusters. II. Kinetic model," *Phys. Plasmas*, Vol. 23, No. 5, 2016, pp. 053503.